

RSC Advances



This is an *Accepted Manuscript*, which has been through the Royal Society of Chemistry peer review process and has been accepted for publication.

Accepted Manuscripts are published online shortly after acceptance, before technical editing, formatting and proof reading. Using this free service, authors can make their results available to the community, in citable form, before we publish the edited article. This *Accepted Manuscript* will be replaced by the edited, formatted and paginated article as soon as this is available.

You can find more information about *Accepted Manuscripts* in the [Information for Authors](#).

Please note that technical editing may introduce minor changes to the text and/or graphics, which may alter content. The journal's standard [Terms & Conditions](#) and the [Ethical guidelines](#) still apply. In no event shall the Royal Society of Chemistry be held responsible for any errors or omissions in this *Accepted Manuscript* or any consequences arising from the use of any information it contains.

Carbon-Coated Ni₃Sn₂ Nanoparticles Embedded in Porous Carbon Nanosheets as Lithium Ion Battery Anode with Outstanding Cycling Stability†

Jian Qin ^a, Xiang Zhang ^a, Naiqin Zhao ^{a, b}, Chunsheng Shi ^a, Enzuo Liu ^a, Jiajun Li ^a, and Chunnian He ^{a, b, *}

Abstract

Carbon-coated Ni₃Sn₂ nanoparticles uniformly embedded in two-dimensional porous carbon nanosheets (2D Ni₃Sn₂@C@PGC) as superior lithium ion battery anode material have been fabricated by a facile and scalable method, which involves *in-situ* synthesis of 2D Ni@C@PGC and chemical vapor transformation processes from 2D Ni@C@PGC to Ni₃Sn₂@C@PGC. With the assistance of water-soluble cubic NaCl template, 2D Ni@C@PGC was firstly *in-situ* synthesized on the surface of NaCl particles. After vapor transformation with SnCl₂, the Ni@C@PGC nanosheets can be converted to Ni₃Sn₂@C@PGC, in which uniform Ni₃Sn₂ nanoparticles coated with conformal graphitized carbon layers are homogeneously embedded in 2D high-conducting carbon nanosheets with a thickness of about 30 nm. This unique 2D dual encapsulation structure with high porosity, high electronic conductivity, outstanding mechanical flexibility and short lithium ion diffusion pathway is very favorable for lithium insertion and extraction during deep charge/discharge process. As a result, the electrode fabricated using 2D Ni₃Sn₂@C@PGC as anode and lithium plate as cathode exhibits a high reversible capacity up to 585.3 mAh/g at a current density of 0.2 C (1 C = 570 mAh/g) after 100 cycles, a high rate capability (484, 424, 378, 314 and 188 mAh/g at 0.2, 0.5, 1, 2 and 5 C, respectively, 1 C = 570 mAh/g), and superior cycling stability at a high rate (350.3 mAh/g at a rate of 1 C after 180 cycles).

^a School of Materials Science and Engineering and Tianjin Key Laboratory of Composites and Functional Materials, Tianjin University, Tianjin 300072, China

^b Collaborative Innovation Center of Chemical Science and Engineering, Tianjin 300072, China
Email: cnhe08@tju.edu.cn

† Electronic supplementary information (ESI) available.

Keywords: Ni₃Sn₂; Carbon nanosheets; Carbon-encapsulated; Lithium ion battery anode; Chemical vapor transformation

1. Introduction

Rechargeable lithium ion batteries (LIBs) are one of the favorite energy storage devices applied from mobile phone to on-going researching hybrid vehicle.^{1,2} Up to now, graphite is widely used as commercial anode materials due to its low-cost, good conductivity and electrochemical stability. However, with limited theoretical capacity of 372 mAh/g (LiC_6), graphite cannot meet the urgent requirement of LIBs with high energy density and power density any more. Therefore, there is extensive interest in the pursuit of high-capacity anode materials. Lithium alloys (LAs), such as Sn, Ge, Sb and etc, which have large theoretical capacity and high electrical conductivity,³⁻¹⁰ have been extensively explored as alternative anode materials for high-performance LIBs. For example, metallic Sn, reversibly transforms between $\text{Li}_{4.4}\text{Sn}$ and Sn in the lithiation/delithiation processes, which can bring a theoretical specific capacity of 992 mAh/g ($\text{Li}_{4.4}\text{Sn}$) based on calculation.¹¹ Despite of those intriguing features, the main obstacle in developing LA-based anodes lies in their dramatic volume change associated with the lithium ion insertion/extraction processes, which would result in their pulverization and exfoliation from the current collector, thereby leading to poor cycling stability.^{12,13}

In order to address these challenges, several approaches have been developed. The first route, so-called nanostructuring, relies on the creation of short diffusion paths for lithium ion transport and free space to accommodate the large volume change.¹⁴⁻¹⁸ Although the nanostructured materials can accommodate the mechanical strain of lithium ion insertion/extraction much better than that of bulk materials, the limited structural stability of the nanostructured LAs remains problematic. Without protection, bare LA nanostructures cannot maintain their original morphology due to the pulverization resulting from the repeated lithiation/delithiation. The second approach is to synthesize active/inactive M_1M_2 intermetallics, in which the electrochemically active metal M_1 (Sn, Ge, Sb) forms the desired lithium alloy, LiM_1 , while the other metal M_2 (Co, Fe, Ni, etc) acts as an electrochemically inactive matrix to absorb the massive volume changes occurring upon the lithiation/delithiation processes as well as serve as an electrical conductor to enhance the electrical integration in the anode.¹⁹⁻²³ Although the large volume change of LAs upon lithium insertion can be accommodated to a limited extent by these buffer matrices, the internal stress in active materials induced by volume expansion cannot be effectively eliminated, leading to the electrodes suffering from serious stress-induced cracking and in turn resulting in

capacity fading after prolonged cycling.^{24,25} The third approach, known as constructing hybrid electrodes composed of LAs and nanostructured carbon with specific structure, aims to improve the structural stability through employing carbon as the protective coating layer or matrix.⁶⁻¹⁰ The carbon layer or matrix serves three main purposes: 1) to wire the active LAs, 2) to buffer the volume change and prevent the aggregation of pulverized active material, and 3) to protect the LAs against direct contact with the electrolyte which may result in the formation of an unstable solid electrolyte interphase (SEI) film. However, because this design does not provide appropriate space to accommodate the large volume expansion, the carbon layer may fracture upon repeated lithiation/delithiation, leading to electrical disconnection, re-exposure of the active materials to electrolyte, and active material aggregation. In addition, formulating a uniform carbon coating onto each metal surface is also impossible in the molecular dimension, which poses problems.

Recently, two-dimensional (2D) nanostructures have attracted tremendous attention owing to their fascinating physical and chemical properties.²⁶⁻³⁰ In particular, the development of graphene and transitional metal oxide nanostructures have been intensively pursued on the basis of fundamental scientific interest coupled with the wide potential for many technological applications. Generally speaking, the 2D nanostructure exhibits unique mechanical, electrical, and optical properties due to the large surface area and miniscule atomic scale thicknesses. In this context, the 2D nanostructures used as LIB electrodes may exhibit much improved kinetics due to their shortened pathway for lithium ion diffusion and large exposed surface offered more lithium-insertion channels.³¹⁻³³

In this work, we take the advantages of nanostructuring, alloying, core/shell encapsulation structures and 2D nanostructured design for preparing discrete, homogeneous and ultrasmall carbon-encapsulated Ni₃Sn₂ nanoparticles embedded in 2D porous graphitic carbon nanosheets (indicated with 2D Ni₃Sn₂@C@PGC nanosheets) as a superior LIB anode. The novel strategy involves *in-situ* preparation of carbon-encapsulated Ni nanoparticles embedded in porous graphitic carbon nanosheets (Ni@C@PGC) with the assistance of the catalytic ability of Ni particles and the surface of NaCl template,¹⁰ and substitution of partial Ni with Sn to form Ni₃Sn₂ (inactive/active intermetallic) nanoparticles through chemical vapor transformation (CVT) method.³⁴⁻³⁶ In this unique dual encapsulated structure, i.e. graphitic onion-like carbon coated Ni₃Sn₂ nanoparticles encapsulated in 2D porous carbon nanosheets, the onion-like carbon shells can

effectively prevent Ni_3Sn_2 nanoparticles from aggregation as well as direct exposure to electrolyte, which is very favorable for maintaining the structural and interfacial stabilization of Ni_3Sn_2 nanoparticles. Meanwhile, the flexible and conductive graphitic carbon nanosheets with high porosity can not only accommodate the mechanical stress caused by volume change of Ni_3Sn_2 nanoparticles but also provide high surface area and short diffusion pathway for the transfer of lithium ions and electrons, which are very beneficial for maintaining structural and electrical integrity of the overall electrode during the charge/discharge processes.¹⁰ As a result, this novel 2D $\text{Ni}_3\text{Sn}_2@\text{C}@\text{PGC}$ nanosheet electrode exhibits tremendously improved lithium storage performance compared with previous NiSn-based anode materials and NiSn/carbon hybrid anodes. It shows a high reversible capacity up to 585.3 mAh/g at a current density of 0.2 C (1 C = 570 mAh/g) after 100 cycles, a high rate capability (484, 424, 378, 314 and 188 mAh/g at 0.2, 0.5, 1, 2 and 5 C, respectively, 1C = 570 mAh/g), and superior cycling performance at a high rate (350.3 mAh/g at a rate of 1 C after 180 cycles).

2. Experimental

2.1 Synthesis of 2D $\text{Ni}_3\text{Sn}_2@\text{C}@\text{PGC}$ nanosheets

During the fabrication process of 2D $\text{Ni}_3\text{Sn}_2@\text{C}@\text{PGC}$ nanosheets, the metal precursors of $\text{Ni}(\text{NO}_3)_2 \cdot 6\text{H}_2\text{O}$ (0.99g), citric acid (2.5 g), and sodium chloride (15 g) were dissolved in 50 mL of deionized water. The resulting mixed solution was dried in a drying oven at 80 °C for 24 h and then grounded by agate mortar to obtain very fine composites powders. After that, the composite powders (10g) together with $\text{SnCl}_2 \cdot 2\text{H}_2\text{O}$ powders (1g) were placed one centimeters apart in a tube furnace and heated at a speed of 5 °C/min to 750 °C, and then kept at 750 °C for 2h under Ar (100 mL/min). Once cooled to room temperature, the as-synthesized product was washed with deionized water for several times to dissolve the sodium chloride and Ni salt, and then pure 2D $\text{Ni}_3\text{Sn}_2@\text{C}@\text{PGC}$ nanosheets were obtained. For comparison, $\text{Ni}_3\text{Sn}_2/\text{C}$ nanoblocks were also synthesized by the same procedures as those for the preparation of the 2D $\text{Ni}_3\text{Sn}_2@\text{C}@\text{PGC}$ nanosheets without using NaCl.

2.2 Characterization techniques

Transmission electron microscope (TEM) and high-resolution TEM (HRTEM) were performed on a FEI Tecnai G² F20 TEM. Raman spectrum was recorded on the LabRAM HR

Raman spectrometer using laser excitation at 514.5 nm from an argon ion laser source. X-ray diffraction (XRD) measurements were taken on a Rigaku D/max diffractometer with Cu KR radiation. Thermogravimetric analysis (TGA) was performed with a Perkin-Elmer (TA Instruments) up to 800 °C at a heating rate of 10 °C/min in air. Brunauer Emmett Teller (BET) surface areas and porosities of the products were determined by nitrogen adsorption and desorption using a Micromeritics ASAP 2020 analyzer.

2.5 Electrochemical measurements

The working electrodes were made through the following steps: active materials (2D Ni₃Sn₂@C@PGC nanosheets, Ni₃Sn₂/C nanoblocks), conductivity agent (carbon black), and binder (polyvinylidene fluoride, PVDF) in a weight ratio of 80:10:10 were blended with N-methylpyrrolidone as solvent. Electrode film prepared by coating the mixture on a copper foil was first vacuum-dried at 80 °C for 0.5h and then at 120 °C for 12 h. Coin cells (CR2032) were fabricated using lithium metal as the counter electrode, Celgard 2400 as the separator, and LiPF₆ (1 M) in ethylene carbonate/ dimethyl carbonate/diethyl carbonate (EC/DMC/DEC, 1:1:1 vol %) as the electrolyte. The assembly of the cell was conducted in an Ar-filled glove box followed by an overnight aging treatment before the test. Cyclic voltammetry (CV) measurement was conducted at 0.1 mV/s within the range of 0.05-3.0 V on a CHI660D electrochemical workstation. The cycling performance and rate capability of the cells were tested within a fixed voltage window of 0.005-3.00 V (vs. Li⁺/Li) by using a battery testing system (LAND CT 2001A, China) at room temperature. All of the specific capacities here were calculated on the basis of the total weight of 2D Ni₃Sn₂@C@PGC nanosheets, Ni₃Sn₂/C nanoblocks. Electrochemical impedance spectroscopy (EIS) measurements were performed using a CHI660D electrochemical workstation by employing an ac voltage of 5 mV amplitude in the frequency range 0.1-100 kHz.³⁹

3. Results and discussion

3.1. Structural and morphological results

Our approach for fabricating 2D Ni₃Sn₂@C@PGC nanosheets principally consists of only one step as illustrated in Figure 1. In a typical synthesis, NaCl, Ni(NO₃)₂·6H₂O and citric acid were mixed to form a homogeneous aqueous solution, and the resulting mixed solution was dried and then ground to obtain very fine composite powders.¹⁰ During this process, the NaCl particles

were uniformly coated with an ultrathin $\text{Ni}(\text{NO}_3)_2 \cdot 6\text{H}_2\text{O}$ -citric acid complex (as shown in Figure S1a), which was induced by the chelation between metal ions and the functional groups of citric acid. After that, the composite powders together with $\text{SnCl}_2 \cdot 2\text{H}_2\text{O}$ powders (put the two powders into the tube furnace one centimeter apart, not mixture) were calcined under Ar. During the calcining process at lower temperature ($<600\text{ }^\circ\text{C}$), the metal precursor ($\text{Ni}(\text{NO}_3)_2 \cdot 6\text{H}_2\text{O}$) is decomposed to nickel oxide, and the carbon species from $\text{C}_6\text{H}_{12}\text{O}_6$ can reduce nickel oxide to Ni nanoparticles, ^{37, 38} which can catalyze the carbon from $\text{C}_6\text{H}_{12}\text{O}_6$ to form encapsulating carbon layer around Ni nanoparticles or porous graphitic carbon. As a result, the coating layer on the surface of the NaCl particles was converted to carbon-encapsulated Ni nanoparticles embedded in a porous graphitic carbon nanosheet with uniform thickness (Figure S1b). When the calcining temperature was risen above the evaporating point ($623\text{ }^\circ\text{C}$) of SnCl_2 , the SnCl_2 vapor could be carried by Ar into the $\text{Ni}@C@PGC$ nanosheets to exchange with Ni and then 2D $\text{Ni}_3\text{Sn}_2@C@PGC$ nanosheets were obtained. In order to verify this process, we have also done the above experiments at $600\text{ }^\circ\text{C}$ (lower than the evaporating point of SnCl_2) and found that only $\text{Ni}@C@PGC$ nanosheets were obtained, as shown in Figure S2, further indicating that $\text{Ni}@C@PGC$ nanosheets have not exchanged with SnCl_2 during the calcining process at a lower temperature.

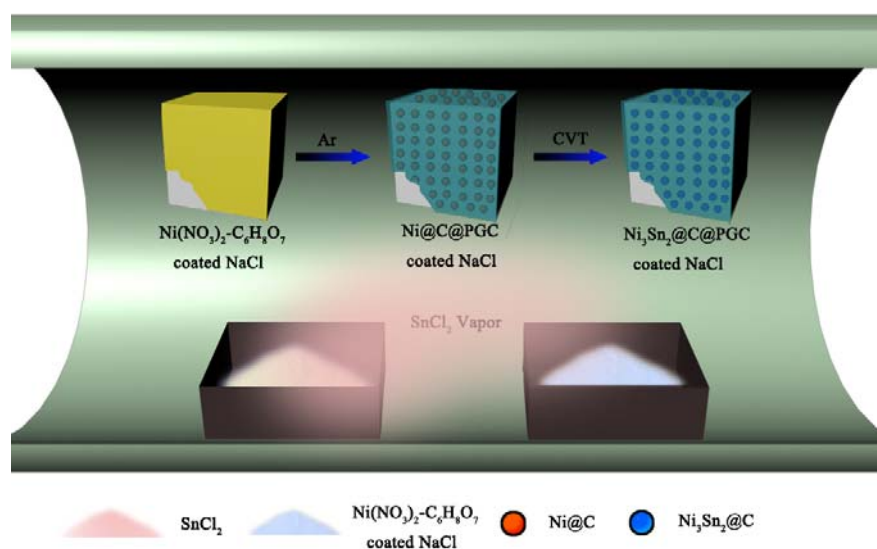


Figure 1. Schematic illustration of the *in-situ* CVT process for one-step synthesizing 2D $\text{Ni}_3\text{Sn}_2@C@PGC$ nanosheets using the surface of NaCl as a template

The crystalline structure of the 2D $\text{Ni}_3\text{Sn}_2@\text{C}@\text{PGC}$ was investigated by XRD (as shown in Figure 2a). The majority of the diffraction peaks, especially for those with high intensity, can be assigned to Ni_3Sn_2 (JCPDS 06-0414), while a small diffraction peaks at 26.2° from graphitic carbon can also be observed, suggesting a total conversion from pre-products ($\text{Ni}@\text{C}@\text{PGC}$ nanosheets) to the target sample (2D $\text{Ni}_3\text{Sn}_2@\text{C}@\text{PGC}$ nanosheets). The sharpness of the diffraction peaks also implies that the metallic phase in the products is well-crystallized. In addition, no diffraction peaks from NaCl and Ni salt can be detected, indicating that the NaCl and Ni salt can be removed completely by water washing. The chemical composition of 2D $\text{Ni}_3\text{Sn}_2@\text{C}@\text{PGC}$ nanosheets was investigated by TGA in air at a heating rate of $10^\circ\text{C}/\text{min}$ and the result is shown in Figure 2b. The sample was heated up to 800°C so that Ni_3Sn_2 can be oxidized to NiO and SnO_2 completely and carbon was oxidized to CO_2 (Figure S3). According to the final content of metal oxide, the original content of Ni_3Sn_2 was calculated to be 60.07% by weight.

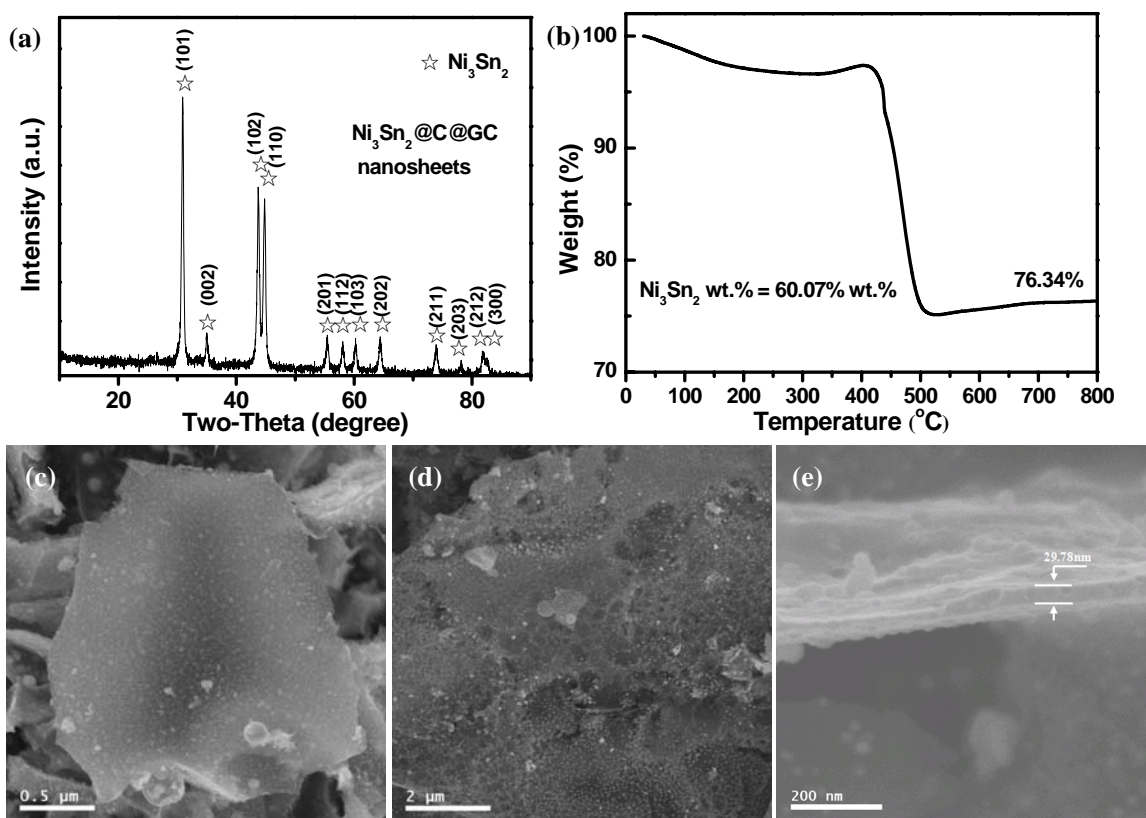


Figure 2. (a) XRD pattern, (b) TGA profile and (c)-(e) SEM images of 2D $\text{Ni}_3\text{Sn}_2@\text{C}@\text{PGC}$ nanosheets.

The morphology and microstructure of 2D $\text{Ni}_3\text{Sn}_2@\text{C}@\text{PGC}$ nanosheets were investigated by SEM and TEM. Representative SEM images of the as-synthesized $\text{Ni}_3\text{Sn}_2@\text{C}@\text{PGC}$ sample are shown in Figure 2c-e. Low-magnification SEM images (Figure 2c and d) indicate that the products have a predominantly 2D nanosheet and porous morphology, in which Ni_3Sn_2 nanoparticles were homogeneously embedded. High-magnification SEM image of Figure 2e shows that the thickness of 2D $\text{Ni}_3\text{Sn}_2@\text{C}@\text{PGC}$ nanosheets is about 30 nm. However, when we performed calcination experiments of the composite powders without NaCl, it was found that 3D nanoblocks with large Ni_3Sn_2 particles embedded were obtained (as shown in Figure S4), which demonstrates that the surface of water-soluble cubic NaCl can be effectively used as template for synthesizing 2D nanostructures.^{10, 39-41} In addition, influence of the amount of NaCl in precursor on 2D nanosheet structures has been investigated, and the results are shown in Figure S5. It can be observed that relatively thicker nanosheets and much larger Ni_3Sn_2 particles with severe aggregation embedded in the nanosheets were obtained at half amount of NaCl in precursor, indicating that the thickness of 2D nanosheets can be adjusted by controlling the amount of NaCl in precursor.^{42, 43} Figure 3a and b show the TEM images of 2D $\text{Ni}_3\text{Sn}_2@\text{C}@\text{PGC}$ nanosheets, we can see that well-dispersed and uniform Ni_3Sn_2 nanoparticles (5~30 nm), which are in a nearly spherical shape, are homogeneously embedded in 2D nanosheets. It is also noticed that these Ni_3Sn_2 nanoparticles are not agglomerated at all by the coalescence of the outer shells although many papers have mentioned that magnetostatic energy of magnetic nanoparticles can be minimized by such coalescence.^{44, 45} Except for the $\text{Ni}_3\text{Sn}_2@\text{C}@\text{PGC}$ nanosheets, other products such as carbon nanotubes or fibers and carbon nanoparticles without encapsulation of the metal were scarcely observed in this work. Figure 3c shows a HRTEM image of 2D $\text{Ni}_3\text{Sn}_2@\text{C}@\text{PGC}$ nanosheets. It clearly reveals that the Ni_3Sn_2 nanoparticles (5~30 nm), which are highly crystallized and uniformly coated with well-graphitized onion-like carbon shells with a thickness of about 2 nm, are evenly embedded in the 2D porous carbon nanosheets. The well-maintained 2D structure demonstrates that the SnCl_2 vapor could effectively diffuse into the nanosheets and penetrate the outer carbon shells to exchange with Ni core without damaging the structure of 2D nanosheets. EDS (Figure S6), EDX (Figure S7) and selected area electronic diffraction (SAED) (inset of Figure 3e) investigations further verify the encapsulated core being Ni_3Sn_2 nanoparticle,

in perfect accordance with above XRD results.

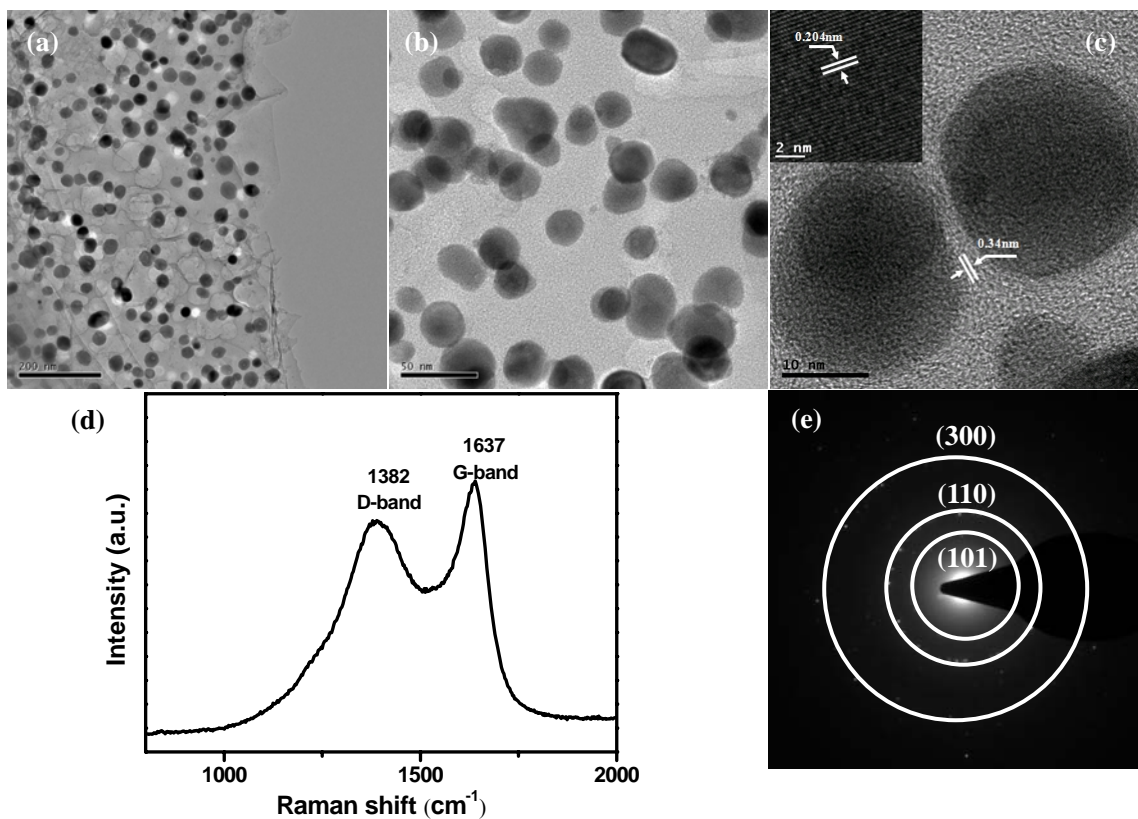


Figure 3. (a) (b) TEM images, (c) HRTEM image of $\text{Ni}_3\text{Sn}_2@\text{C}@\text{PGC}$ nanosheet. (d) Raman spectrum and (e) diffraction pattern of $\text{Ni}_3\text{Sn}_2@\text{C}@\text{PGC}$ nanosheet.

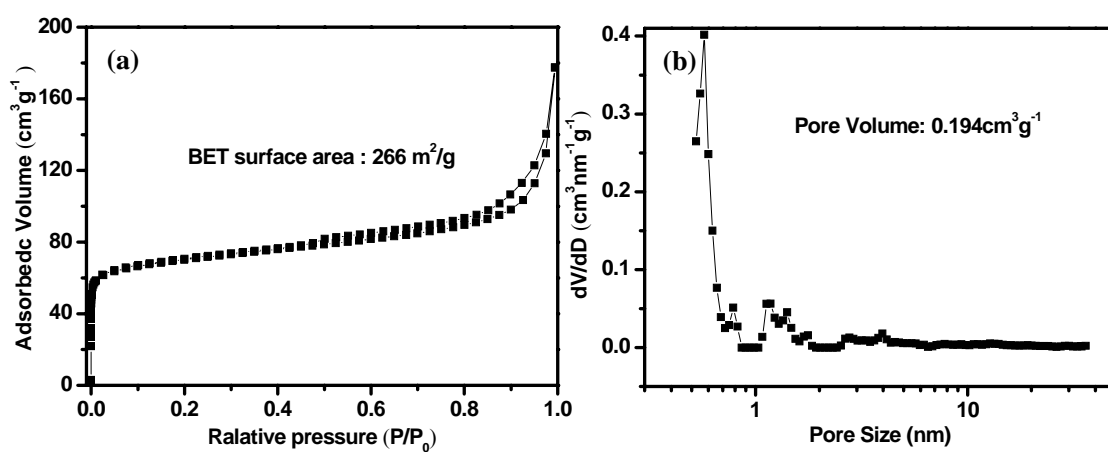


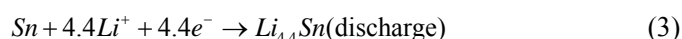
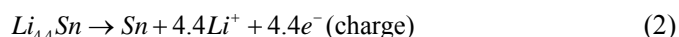
Figure 4. (a) Nitrogen adsorption–desorption isotherms and (b) pore distribution analysis by DFT method of $\text{Ni}_3\text{Sn}_2@\text{C}@\text{PGC}$ nanosheet.

The 2D Ni₃Sn₂@C@PGC nanosheets were also characterized by Raman spectroscopy in detail to further estimate the ordering degree of carbon structure in the nanosheets. Typical Raman spectrum collected within the 800–2000 cm⁻¹ range is shown in Figure 3(d). It can be seen that the spectrum exhibits two obvious peaks, corresponding to the *D* band (1382 cm⁻¹) and *G* band (1637 cm⁻¹), respectively. Definitely, the former band (*D* band) is associated with edges, defects, and disordered carbon, whereas the latter band (*G* band) is ascribed to *sp*²-hybridized carbon.⁴⁶ It is well known that the intensity ratio of *G* peak to *D* peak (*I*_G/*I*_D) is widely used to assess the crystallization of carbon materials. The *I*_G/*I*_D ratio of our 2D Ni₃Sn₂@C@PGC nanosheets was calculated to be ~1.16, implying that the carbon in the nanosheets we obtained is well-crystallized graphitic carbon, which will be very beneficial for enhancing the electronic conduction of the overall electrode. Nitrogen adsorption-desorption measurements are carried out at 77 K to study the textural characteristics of the 2D Ni₃Sn₂@C@PGC nanosheets. For comparison, the Ni₃Sn₂/C nanoblocks were also characterized by Nitrogen adsorption-desorption measurements. As shown in Figure 4, the isotherm profile of the 2D Ni₃Sn₂@C@PGC nanosheets exhibits a typical IV isotherm with a hysteresis loop in the *P*/*P*₀ range of 0.5–0.9, indicating that the pores inside the sample consist of micropores and mesopores, as further verified by the pore size distribution in Fig. 4d. The BET specific surface area of our 2D Ni₃Sn₂@C@PGC nanosheets is measured to be 266 m²/g, which is much higher than that of Ni₃Sn₂/C nanoblocks (about 51.5 m²/g) (see Figure S8). The pore size distribution (as shown in Figure 4b) of the 2D Ni₃Sn₂@C@PGC nanosheets analyzed by DFT method lies in 0.5-50 nm range, which includes micropores and mesopores. The pore volume of the product determined by the Barrett-Joyner-Halenda method is 0.194 cm³/g. This porous structure consisting of micropores and mesopores with the size in the range of 0.5-50 nm may be attributed to the escape of small molecule in citric acid during calcining and no doubt that will be of great benefit to the electrolyte ion diffusion to active sites with less resistance and tolerate the volume change of the NiSn nanocrystals during charge/discharge cycles.^{10, 39}

3.2. Electrochemical performance of the 2D Ni₃Sn₂@C@PGC Nanosheets

The lithium insertion/extraction reactions of the 2D Ni₃Sn₂@C@PGC nanosheets were first investigated by CV experiment as shown in Figure 5a. The test was carried out at a scanning rate of 0.1 mV/s within the voltages window of 0.005-3 V (vs. Li/Li⁺). In the first scanning cycle, two

cathodic peaks between 0.5-1 V and 1.5-1.75 V respectively could be observed, but disappeared completely in the second cycle. This can be attributed to some irreversible reactions associated with the formation of SEI film as well as the decomposition of electrolyte. The cathodic peak between 0-0.5 V and anodic peaks at 0.68 V, 1.3 V and 2.1 V are corresponding to the electrochemical alloying/dealloying reactions. The whole reaction is expected to evolve like this:



While the reaction (1) occurs in the first activation cycle (irreversible), and reaction (2), (3) alternately operate in the following cycles. In addition, it should be noted that from the 2nd to the 5th cycle in our results, the profiles almost overlapped, indicating the perfect reversibility of our electrode.

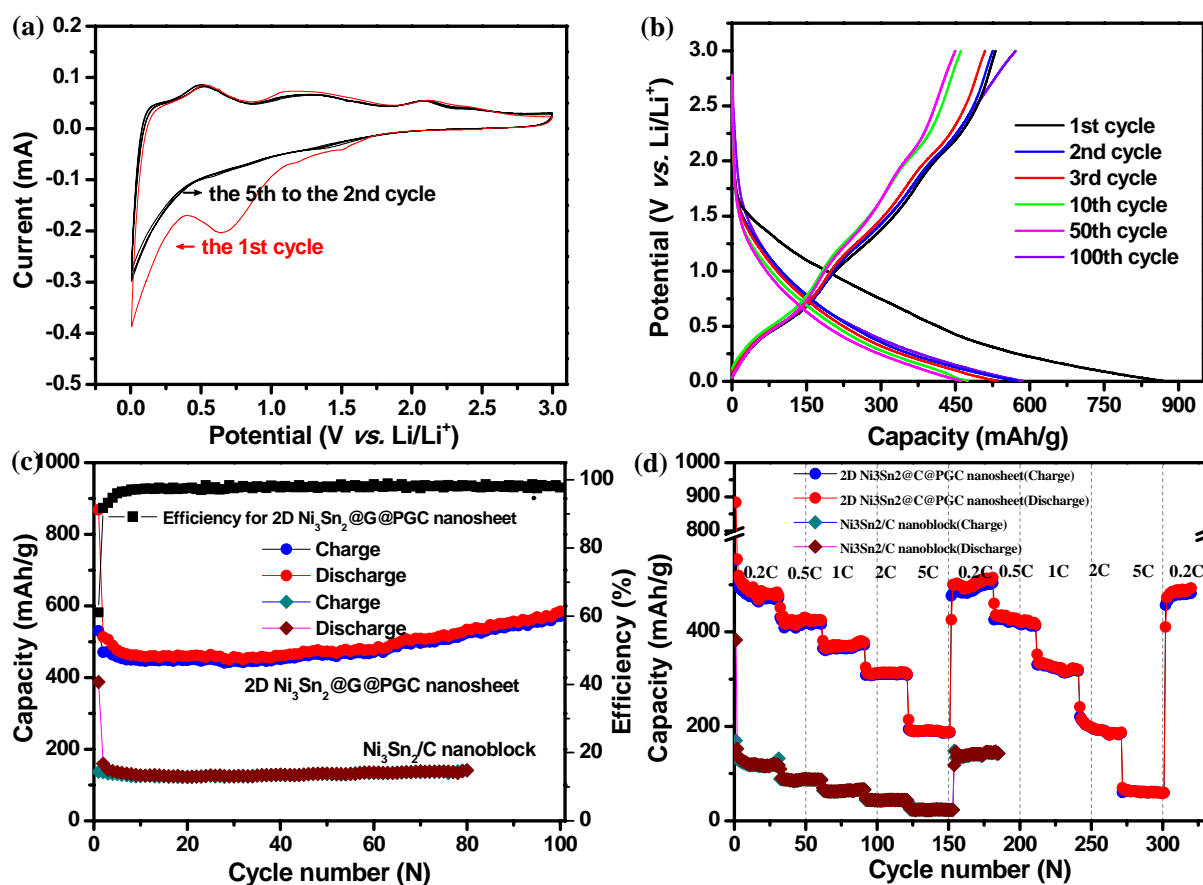


Figure 5. (a) CV curves of the 2D Ni₃Sn₂@C@PGC electrode at a voltage range of 0.005 to 3.0 V

and scan rate of 0.1 mV/s. (b) Voltage profiles of the 2D $\text{Ni}_3\text{Sn}_2@\text{C}@\text{PGC}$ electrode at a current density of 0.2 C. (c) Cycle performance of the 2D $\text{Ni}_3\text{Sn}_2@\text{C}@\text{PGC}$ and $\text{Ni}_3\text{Sn}_2/\text{C}$ nanoblocks at a current density of 0.2 C (1 C = 570 mAh/g). (d) Rate cycle performance of the electrodes of 2D $\text{Ni}_3\text{Sn}_2@\text{C}@\text{PGC}$ and $\text{Ni}_3\text{Sn}_2/\text{C}$ nanoblocks at charge/discharge rates from 0.2 to 5 C for 320 cycles.

Representative galvanostatic charge-discharge profiles of 2D $\text{Ni}_3\text{Sn}_2@\text{C}@\text{PGC}$ nanosheets at a current density of 0.2 C (1 C = 570 mAh/g) are shown in Figure 5(b). The first lithiation process delivers an initial discharge capacity of 868.8 mAh/g, and the subsequent delithiation delivers a charge capacity of 531 mAh/g, resulting in a Coulombic efficiency of 61.1%. The relatively low initial Coulombic efficiency observed in the first cycle may be attributed to the irreversible capacity loss, including inevitable formation of SEI and decomposition of electrolyte, which are common to most anode materials³⁻¹⁰ and also agree well with the above CV results that the cathodic peaks are present in the first scan while absent afterward. A prelithiation strategy can be used to improve the low Coulombic efficiency in practical application. The Coulombic efficiency increases dramatically to 96% in the fifth cycle and levels off at 98~100% in subsequent cycles, indicating a facile insertion/extraction of lithium ions and efficient transportation of electrons and ions in this nanosheet anode. Importantly, it should be noted that both charge and discharge profiles exhibit little shift from the second to the 100 cycles, further verifying that the 2D $\text{Ni}_3\text{Sn}_2@\text{C}@\text{PGC}$ nanosheet electrodes are very stable during cycling.

The cycling performances of 2D $\text{Ni}_3\text{Sn}_2@\text{C}@\text{PGC}$ nanosheets and $\text{Ni}_3\text{Sn}_2/\text{C}$ nanoblocks produced without using NaCl at a current density of 0.2 C are shown in Figure 5(c). It is evident that the 2D $\text{Ni}_3\text{Sn}_2@\text{C}@\text{PGC}$ nanosheet electrode shows superior cycling stability and exhibits almost completely stable cycling performance from the second cycle onwards. Even after 100 cycles, a higher capacity of 585.3 mAh/g can be maintained, which is 113% of the capacity at the second cycle. The capacity rise of the $\text{Ni}_3\text{Sn}_2@\text{C}@\text{PGC}$ composite is commonly observed for lithium alloy/carbon composite anodes, and normally attributed to the presence of a possible activation process in the electrode.⁴⁷⁻⁴⁹ In sharp contrast, the $\text{Ni}_3\text{Sn}_2/\text{C}$ nanoblocks electrode only delivers a first discharge and charge capacity of 388mAh/g and 137mAh/g respectively, and is stable at only 141.4mAh/g after 80 cycles. Therefore, the 2D $\text{Ni}_3\text{Sn}_2@\text{C}@\text{PGC}$ nanosheet anode

demonstrates a remarkably high reversible capacity and superior cycle performance. This may be largely ascribed to the unique 2D dual carbon-encapsulated structure we have built, that is, graphitic onion-like carbon-coated Ni_3Sn_2 nanoparticles embedded in 2D porous carbon nanosheets. During the charge/discharge process, the onion-like carbon shells around Ni_3Sn_2 nanoparticles not only can effectively prevent active metal materials from immediate contacting with the electrolyte and thus decrease the side reactions occurred on the surface of active metal materials, but also can restrain the agglomeration of Ni_3Sn_2 nanoparticles to large particles during cycling.^{10,39} As for the 2D porous carbon nanosheets with high mechanical flexibility, they can relieve the mechanical stress caused by the volume change of Ni_3Sn_2 nanoparticles and also can act as a stable matrix for SEI film formation, which are very helpful for enhancing the cycling stability. In addition, the 2D carbon nanosheets with a porous feature and integrative characteristic can lead to a high contact area between the electrode and electrolyte and a much shorter pathway for lithium ion diffusion, which are very beneficial for the efficient access of electrolyte into the electrode interior to guarantee a rapid lithium ion insertion/extraction reaction. All these advantages discussed above result in high capacities and outstanding cycle stability.

Figure 5(d) demonstrates the rate and rate cycle performance of 2D $\text{Ni}_3\text{Sn}_2@\text{C}@PGC$ nanosheets and $\text{Ni}_3\text{Sn}_2/\text{C}$ nanoblocks at different current rates (from 0.2 C to 5 C). It can be seen that the 2D $\text{Ni}_3\text{Sn}_2@\text{C}@PGC$ nanosheets exhibit a durable and stable rate capacity at different charge/discharge rates. In the first rate cycle, the average reversible capacities are 484, 424, 378, 314 and 188 mAh/g at the rates of 0.2 (step 1), 0.5 (step2), 1 (step3), 2 (step4) and 5 C (step5), respectively, and the corresponding power and energy densities for different charge/discharge rates are demonstrated in the Ragone plot of Figure S9. This excellent rate performance is superior to most Sn-based alloy anode materials.^{23,50-58} When the current rate returns to the initial 0.2 C after 150 cycles, a capacity of as high as 500 mAh/g is still recoverable and sustainable up to the 180th cycle, which is even higher than the initial capacity of 484 mAh/g. This indicates that our nanosheet structure is stable enough so that even cycled at a high rate of 5 C, charging/discharging processes finished within 8min, still can maintain the structural integrity. Moreover, we have performed again the whole rates (from 180 cycles to 320 cycles) to further measure the rate cycle performance (as shown in Figure 5d). It is obvious that within 320 cycles, the second stage of rate cycling (from 180th to 320th cycles) has only slightly shift against the first stage of rate cycling

(from 1st to 180th cycles), as shown in Table S1. When returns back to 0.2C after two rate cycling stages, the electrode still delivers a reversible capacity of 497 mAh/g. The above results indicate that the structure of Ni₃Sn₂@C@PGC nanosheets remains exceedingly stable even under high rate cycling. As a comparison, the Ni₃Sn₂/C nanoblocks electrode produced without using NaCl shows significantly lower capacity (as shown in Figure 5d and Table S1), further verifying the advantages of using the 2D Ni₃Sn₂@C@PGC nanosheets for lithium storage. Figure 6a shows the charge-discharge profiles of 2D Ni₃Sn₂@C@PGC nanosheets at different rates, from which we can see that the curves at high rates are still preserved similar to that at low rates, indicating the very stable structure of 2D Ni₃Sn₂@C@PGC nanosheets even at high charge/discharge rates. Figure 6b shows the cycle performance of our electrode at high rates, the experiment was carried out at current rates of 0.5 C and 1 C (570 mAh/g) within the voltage window between 0.005-3 V. The reversible capacity at 0.5 C after 250 cycles is 538.8 mAh/g, even higher than the initial capacity of 409 mAh/g, which can be attributed to the activation effect and is in line with the 0.2 C cycling performance. Moreover, taken the reversible capacity at 1 C rate in initial cycle (400 mAh/g) and in the 180th cycle (350.3 mAh/g) into account, the capacity retention is as high as 87.5%, and the coulombic efficiency remains above 99%, which further indicate that this interesting nanosheet electrode has superior cycling stability even at very high charge/discharge rates.

In order to illustrate the reasons for the much higher rate performance of the 2D Ni₃Sn₂@C@PGC nanosheets than that of the Ni₃Sn₂/C nanoblocks, EIS measurements of the nanosheets and nanoblocks at fresh coin cells were carried out. As shown in Figure 6c, the two impedance spectra have similar features: a medium-to-high-frequency depressed semicircle and a low-frequency linear tail. The high-frequency semicircle is due to the summation of the contact, the SEI resistance R_f , and the charge-transfer impedance R_{ct} on the electrode/electrolyte interface, and the low-frequency linear tail corresponds to the Warburg impedance (Z_w) associated with the diffusion of lithium ions in the bulk electrode (R_e).^{39, 59, 60} According to Figure 6c, it can be seen clearly that the semicircle diameter of the 2D Ni₃Sn₂@C@PGC electrode is significantly smaller than that of the Ni₃Sn₂/C nanoblocks, implying that the Ni₃Sn₂@C@PGC nanosheets have a much higher electrical conductivity and a much less charge-transfer resistances in the electrode.^{39, 59, 60}

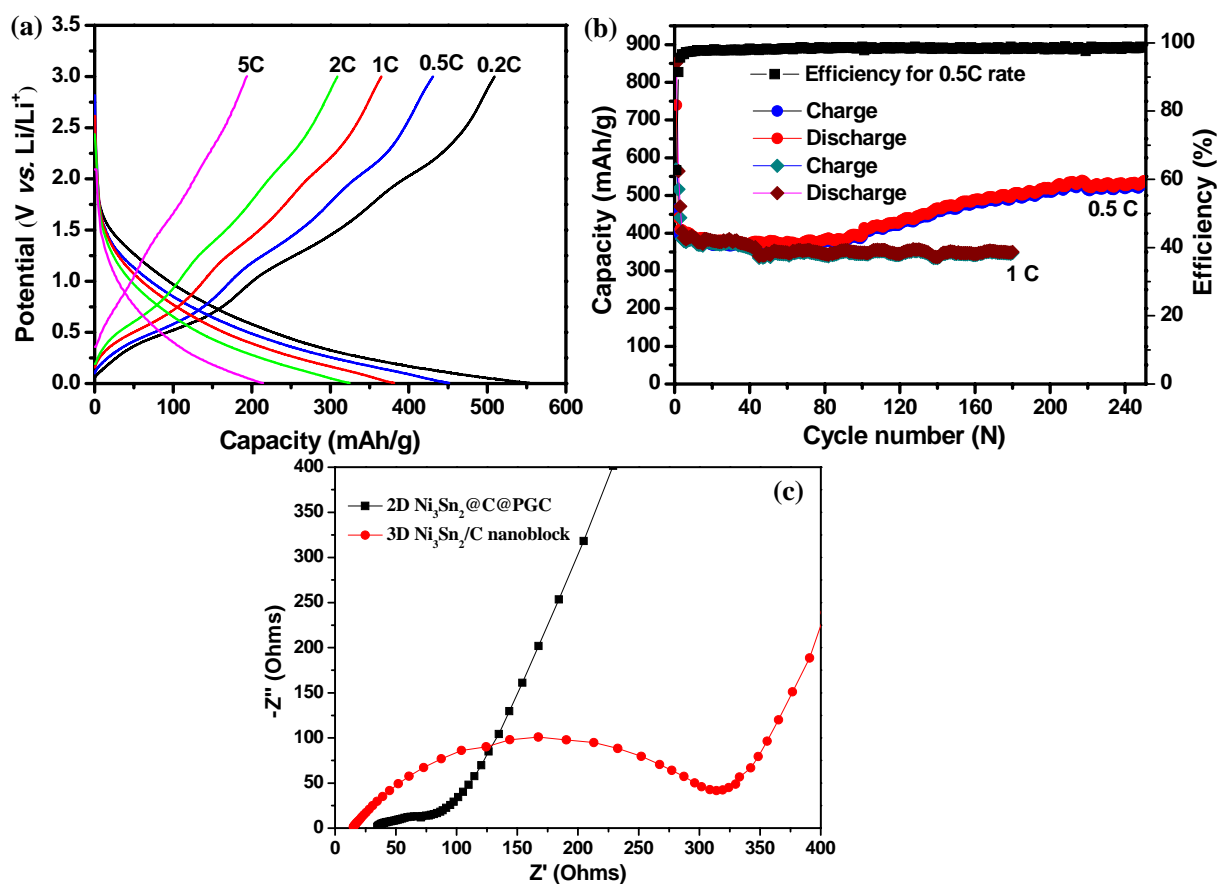


Figure 6. (a) Voltage profiles of the electrodes of 2D Ni₃Sn₂@C@PGC at charge/discharge rates from 0.2 to 5 C. (b) Cycle performance of the 2D Ni₃Sn₂@C@PGC electrode at current densities of 0.5 C or 1 C. (c) Nyquist plots of 2D Ni₃Sn₂@C@PGC and 3D Ni₃Sn₂/C nanoblock at fresh coin cells over the frequency range from 100 kHz to 0.01 Hz.

To disclose the mechanism for the excellent electrochemical performance and structure change of the 2D Ni₃Sn₂@C@PGC nanosheet electrode, the tested cell was disassembled after cycling test, and the morphology and structure of the nanohybrids were investigated by using TEM, as shown in Figure 7. Although the sample is covered with thin SEI film, we can see clearly the Ni₃Sn₂ nanoparticles are still evenly embedded in the 2D carbon nanosheets without any aggregation or pulverization, indicating that the morphology and structure of the nanosheets are well maintained. These results demonstrate that the 2D carbon matrix combined with carbon shells can effectively buffer the volume change of Ni₃Sn₂ as well as suppress the aggregation of Ni₃Sn₂ during cycling, thus preserving the integrity of the overall electrode.

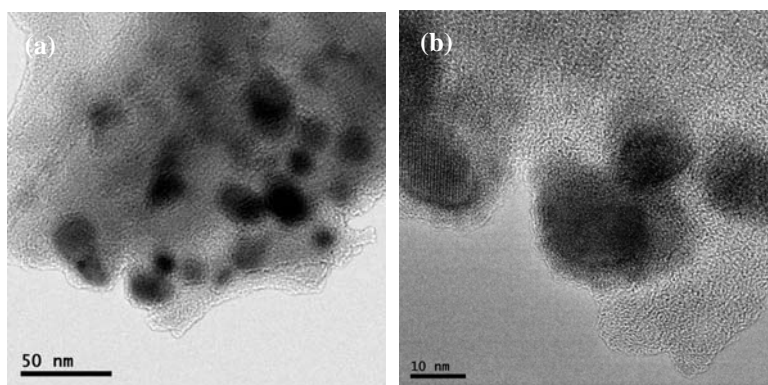


Figure 7. TEM and HRTEM images of 2D $\text{Ni}_3\text{Sn}_2@\text{C}@\text{PGC}$ nanosheets after 100 charge-discharge cycles.

As shown in the results presented above, our 2D $\text{Ni}_3\text{Sn}_2@\text{C}@\text{PGC}$ nanosheets electrode displays superior electrochemical performance and structural stability, which can be attributed to the following factors: (1) The active-inactive Ni_3Sn_2 intermetallic compound. The lithiation of the Sn phase to form $\text{Li}_{x<4.4}\text{Sn}$ would release the metal component Ni to the surrounding environment, and Ni as a matrix can absorb the massive volume changes occurring upon the lithiation/delithiation processes. Uniform distribution of the electrically conducting Ni nanoparticles in close contact to Li_xSn binaries could contribute to the electrical integration in the anode. Moreover, additional Ni phase could also function as an inactive matrix to inhibit Sn aggregation. All these advantages would be very beneficial for achieving outstanding cycling stability. (2) The dual carbon-encapsulated structure. The onion-like carbon shells can effectively prevent Ni_3Sn_2 nanoparticles from aggregation as well as direct exposure to electrolyte, which is very favorable for maintaining the structural and interfacial stabilization of Ni_3Sn_2 nanoparticles.^{10, 39} Meanwhile, the flexible and conductive graphitic carbon nanosheets can accommodate the mechanical stress caused by volume change of Ni_3Sn_2 nanoparticles as well as further assist onion-like carbon shells to inhibit the aggregation of Ni_3Sn_2 nanoparticles and thus maintain the structural and electrical integrity of the $\text{Ni}_3\text{Sn}_2@\text{C}@\text{PGC}$ electrode during the charge and discharge processes. (3) The 2D porous and integrative structure. The 2D integrative feature and porous nature of the nanosheets as thin as only about 30 nm can ensure a large electrode-electrolyte contact area, which can render the easy access of liquid electrolyte into the bulk of the electrode material to provide fast transport channels for the lithium ions and offer

efficient transport pathways for ion diffusion toward the deep portions of the electrodes. Moreover, it would be easy for lithium ions, electrochemically adsorbed on both sides of 2D ultrathin nanosheets, to have high reversible storage capability. In addition, the well-graphitized micrometer-sized carbon nanosheets can form a quite effective and continuous conductive network, which gives rise to a very high electrical conductivity of the overall electrode and is thus highly favorable for improving the rate capability of the $\text{Ni}_3\text{Sn}_2@\text{C}@\text{PGC}$ electrode.^{10, 39} Based on the analyses presented above, we believe our material is of enhanced structural stability and integrity as well as excellent kinetics for lithium ion and charge transportation, thus, the lithium storage property is remarkably improved.

4. Conclusions

In summary, carbon-coated Ni_3Sn_2 nanoparticles embedded in 2D porous carbon nanosheets (2D $\text{Ni}_3\text{Sn}_2@\text{C}@\text{PGC}$) with superior electrochemical performance have been fabricated via a facile and scalable method, which involves *in-situ* synthesis of 2D $\text{Ni}@\text{C}@\text{PGC}$ and chemical vapor transformation processes. This unique hybrid nanostructure consists of very thin 2D porous graphitic carbon nanosheets with a thickness of less than 30 nm, in which Ni_3Sn_2 nanoparticles (5~20 nm) coated with thin onion-like carbon shells (~2 nm) are homogeneously embedded. In this unique dual encapsulation structure, the onion-like carbon shells can effectively prevent Ni_3Sn_2 nanoparticles from aggregation as well as direct exposure to electrolyte and thus maintain the structural and interfacial stabilization of Ni_3Sn_2 nanoparticles. Meanwhile, the flexible and conductive graphitic carbon nanosheets with high porosity can not only accommodate the mechanical stress caused by volume change of Ni_3Sn_2 nanoparticles but also provide high surface area and short diffusion pathway for the transfer of lithium ions and electrons, thereby leading to excellent structural and electrical integrity of the overall electrode during the charge/discharge processes. Therefore, this unique structure demonstrates a high reversible capacity up to 585.3 mAh/g at a current density of 0.2 C (1 C = 570 mAh/g) after 100 cycles, a high rate capability (484, 424, 378, 314 and 188 mAh/g at 0.2, 0.5, 1, 2 and 5 C, respectively), excellent capacity retention rate (about 90% after two periods rate test, a total of 320 cycles), and superior cycling performance at a very high rate (350.3 mAh/g at a high rate of 1C after 180 cycles). Furthermore, the interesting strategy we have exhibited could also be extended to construct many other

two-dimensional materials and carbon-encapsulated structure for important applications in other scientific fields such as supercapacitors, catalysts, fuel cell and sensors.

Acknowledgments

The authors acknowledge the financial support by the National Natural Science Foundation of China (No. 51422104, No. 51472177 and No. 51272173) and Foundation for the Author of National Excellent Doctoral Dissertation of China (No. 201145), Program for New Century Excellent Talents in University (NCET-12-0408), Natural Science Foundation of Tianjin City (No.12JCYBJC11700), Elite Scholar Program of Tianjin University, Innovation Foundation of Tianjin University and National Basic Research Program of China (2010CB934700).

References

- 1 M. Armand and J. M. Tarascon, *Nature* 2008, 451, 652.
- 2 K. Kang, Y. S. Meng, J. Bréger, C. P. Grey and G. Ceder, *Science* 2006, 311, 977.
- 3 B. Wang, X. Li, T. Qiu, B. Luo, J. Ning, J. Li and L. Zhi, *Nano Lett.*, 2013, 13, 5578.
- 4 B. Wang, X. Li, X. Zhang, B. Luo, M. Jin, M. Liang and L. Zhi, *ACS Nano* 2013, 7, 1437.
- 5 D. J. Xue, S. Xin, Y. Yan, K. C. Jiang, Y. X. Yin, Y. G. Guo and L. J. Wan, *J. Am. Chem. Soc.*, 2012, 134, 2512.
- 6 A. M. Chockla, K. C. Klavetter, C. B. Mullins and B. A. Korgel, *Chem. Mater.*, 2012, 24, 3738.
- 7 Y. Yu, L. Gu, C. Zhu, P. A. van Aken and J. Maier, *J. Am. Chem. Soc.*, 2009, 131, 15984.
- 8 Y. Yu, L. Gu, C. Wang, A. Dhanabalan, P. A. van Aken and J. Maier, *Angew. Chem. Int. Edit.*, 2009, 48, 6485.
- 9 Y. Yu, L. Gu, X. Lang, C. Zhu, T. Fujita, M. Chen and J. Maier, *Adv. Mater.*, 2011, 23, 2443.
- 10 J. Qin, C. He, N. Zhao, Z. Wang, C. Shi, E. Z. Liu and J. Li, *ACS Nano*, 2014, 8: 1728.
- 11 I. A. Courtney and J. R. Dahn, *J. Electrochem. Soc.*, 1997, 144, 2045.
- 12 J. Yang, M. Winter and J. O. Besenhard, *Solid State Ionics*, 1996, 90, 281.
- 13 Y. Xu, Q. Liu, Y. Zhu, Y. Liu, A. Langrock, M. R. Zachariah and C. Wang, *Nano Lett.*, 2013, 13, 470.
- 14 R. Hu, M. Zhu, H. Wang, J. Liu and J. Zou, *Acta Mater.*, 2012, 60, 4695.

- 15 K. T. Lee, Y. S. Jung and S. M. Oh, *J. Am. Chem. Soc.*, 2003, 125, 5652.
- 16 Y. Zou and Y. Wang, *ACS Nano*, 2011, 5, 8108.
- 17 B. Wang, B. Luo, X. Li and L. Zhi, *Mater. Today*, 2012, 15, 544.
- 18 W. M. Zhang, J. S. Hu, Y. G. Guo, S. F. Zheng, L. S. Zhong, W. G. Song and L. J. Wan, *Adv. Mater.*, 2008, 20, 1160.
- 19 M. Chamas, M. T. Sougrati, C. Reibel and P. E. Lippens, *Chem. Mater.*, 2013, 25, 2410.
- 20 Y. Gu, F. Wu and Y. Wang, *Adv. Funct. Mater.*, 2013, 23, 893.
- 21 P. Chen, L. Guo and Y. Wang, *J. Power Sources*, 2013, 222, 526.
- 22 J. Hassoun, S. Panero, P. Simon, P. L. Taberna and B. Scrosati, *Adv. Mater.*, 2007, 19, 1632.
- 23 X. L. Wang, W. Q. Han, J. Chen and J. Graetz, *ACS Appl. Mater. Inter.*, 2010, 2, 1548.
- 24 K. Hirai, T. Ichitsubo, T. Uda, A. Miyazaki, S. Yagi and E. Matsubara, *Acta Mater.*, 2008, 56, 1539.
- 25 M. E. Stournara, P. R. Guduru and V. B. Shenoy, *J. Power Sources*, 2012, 208, 165.
- 26 Z. Lu, J. Zhu, D. Sim, W. Zhou, W. Shi, H. H. Hng and Q. Yan, *Chem. Mater.*, 2011, 23, 5293.
- 27 X. Wang, X. L. Wu, Y. G. Guo, Y. Zhong, X. Cao, Y. Ma and J. Yao, *Adv. Funct. Mater.*, 2010, 20, 1680.
- 28 D. Wang, R. Kou, D. Choi, Z. Yang, Z. Nie, J. Li and I. A. Aksay, *ACS Nano* 2010, 4, 1587.
- 29 S. Liu, J. Yu and M. Jaroniec, *Chem. Mater.*, 2011, 23, 4085.
- 30 B. Jang, M. Park, O. B. Chae, S. Park, Y. Kim, S. M. Oh and T. Hyeon, *J. Am. Chem. Soc.*, 2012, 134, 15010.
- 31 J. Liu and X. W. Liu, *Adv. Mater.*, 2012, 24, 4097.
- 32 Z. Pan, N. Liu, L. Fu and Z. Liu, *J. Am. Chem. Soc.*, 2011, 133, 17578.
- 33 S. Yin, Y. Zhang, J. Kong, C. Zou, C. M. Li, X. Lu and X. Chen, *ACS Nano*, 2011, 5, 3831.
- 34 J. Y. Lee, D. S. Kim and J. Park, *Chem. Mater.*, 2007, 19, 4663.
- 35 J. Park, H. Zheng, Y. W. Jun and A. P. Alivisatos, *J. Am. Chem. Soc.*, 2009, 131, 13943.
- 36 M. V. Kovalenko, D. V. Talapin, M. A. Loi, F. Cordella, G. Hesser, M. I. Bodnarchuk and W. Heiss, *Angew. Chem. Int. Edit.*, 2008, 47, 3029.
- 37 Y. M. Chen, X. Y. Li, X. Y. Zhou, H. M. Yao, H. T. Huang, Y. W. Mai and L. M. Zhou, *Energy Environ. Sci.*, 2014, 7, 2689.

- 38 Y. M. Chen, X. Y. Li, K. Park, J. Song, J. H. Hong, L. M. Zhou, Y. W. Mai, H. T. Huang and J. B. Goodenough, *J. Am. Chem. Soc.*, 2013, 135, 16280.
- 39 C. He, S. Wu, N. Zhao, C. Shi, E. Liu and J. Li, *ACS Nano*, 2013, 7, 4459.
- 40 S. Wu, Z. Wang, C. He, N. Zhao, C. Shi, E. Liu and J. Li, *J. Mater. Chem. A*, 2013, 1, 11011.
- 41 L. Chen, Z. Wang, C. He, N. Zhao, C. Shi, E. Liu and J. Li, *ACS Appl. Mater. Inter.*, 2013, 5, 9537.
- 42 G. Derrien, J. Hassoun, S. Panero and B. Scrosati, *Adv. Mater.*, 2007, 19, 2336.
- 43 J. Hassoun, G. Derrien, S. Panero and B. Scrosati, *Adv. Mater.*, 2008, 20, 3169.
- 44 N. Caiulo, C. H. Yu, K. M. K. Yu, C. C. Lo, W. Oduro, B. Thiebaut and S. C. Tsang, *Adv. Funct. Mater.*, 2007, 17, 1392.
- 45 A. A. El-Gendy, V. O. Khavrus, S. Hampel, A. Leonhardt, B. Buchner and R. Klingeler, *J. Phys. Chem. C* 2010, 114, 10745.
- 46 C. H. Huang, R. A. Doong, D. Gu and D. Zhao, *Carbon* 2011, 49, 3055.
- 47 X. F. Li, A. Dhanabalan, L. Gu and C. L. Wang, *Adv. Energy Mater.*, 2012, 2, 238.
- 48 X. F. Li, Y. Zhong, M. Cai, M. P. Balogh, D. N. Wang, Y. Zhang, R. Y. Li and X. L. Sun, *Electrochim. Acta*, 2013, 89, 387.
- 49 Y. H. Xu, J. C. Guo and C. S. Wang, *J. Mater. Chem.*, 2012, 22, 9562.
- 50 J. Hassoun, G. A. Elia, S. Panero and B. Scrosati, *J. Power Sources*, 2011, 196, 7767.
- 51 D. B. Polat, J. Lu, A. Abouimrane, O. Keles and K. Amine, *ACS Appl. Mater. Inter.*, 2014, 6, 10877.
- 52 M. Kotobuki, N. Okada and K. Kanamura, *Chem. Commun.*, 2011, 47, 6144.
- 53 W. J. Cui, F. Li, H. J. Liu, C. X. Wang and Y. Y. Xia, *J. Mater. Chem.*, 2009, 19, 7202.
- 54 B. Feng, J. Xie, G. S. Cao, T. J. Zhu and X. B. Zhao, *NEW J. Chem.*, 2013, 37, 474.
- 55 C. M. Park and K. J. Jeon, *Chem. Commun.*, 2011, 47, 2122.
- 56 X. L. Wang, H. Chen, J. Bai and W. Q. Han, *J. Phys. Chem. Lett.*, 2012, 3, 1488.
- 57 D. H. Nam, R. H. Kim, C. L. Lee and H. S. Kwon, *J. Electrochem. Soc.*, 2012, 159, A1822.
- 58 Y. Wang, P. Zhang, X. Ren and G. Yi, *J. Electrochem. Soc.*, 2011, 158, A1404.
- 59 Y. M. Chen, Z. G. Lu, L. M. Zhou, Y. W. Mai and H. T. Huang, *Nanoscale*, 2012, 4, 6800.
- 60 Y. M. Chen, Z. G. Lu, L. M. Zhou, Y. W. Mai and H. T. Huang, *Energy Environ. Sci.*, 2012, 5, 7898.